Heliyon 9 (2023) e21275

Contents lists available at ScienceDirect

Heliyon

journal homepage: www.cell.com/heliyon

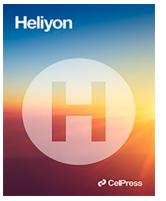

# Experimental study on particle movement and erosion behavior of the elbow in liquid–solid flow

Zhenqiang Xie [a,b,*], Xuewen Cao [b], Qingping Li [a], Haiyuan Yao [a], Rui Qin [a], Xiaoyang Sun [c]

[a] China National Offshore Oil Corporation Research Institute, Beijing, 100028, China
[b] College of Pipeline and Civil Engineering, China University of Petroleum (East China), Qingdao, 266580, China
[c] National Oil and Gas Pipeline Network Group Co Ltd, Beijing, 100028, China

ARTICLE INFO

*Keywords:*
Elbow
Liquid–solid flow
Particle trajectory deviation
Erosion micro-morphology

ABSTRACT

Recent investigations into the erosion of elbow junctions predominantly focus on identifying and predicting peak erosion points. Notably, these studies rely heavily on computational fluid dynamics methods, a valid approach but limited by its lack of empirical physical data. Additionally, the majority of these studies concentrate on the extrados, or outer curve of the elbow, neglecting the intrados or the inner curve. To provide a more comprehensive understanding of particle movements and the micro-mechanics of erosion on the elbow intrados, this study utilizes advanced observational technologies. High-speed camera technology, coupled with scanning electron microscopy, is employed to capture and record particle motion and micro-erosion patterns. The erosion rate is then estimated via the weight-loss method. The findings suggest that in low-speed liquid–solid flows (2.5 m/s), particles released from the intrados side of the elbow inlet exhibit a significant trajectory deviation from the centreline at an elbow angle of 60° from the inlet. Particles released from the extrados deviate towards the intrados side at an elbow angle of 30°. Secondary flow contributes to particle acceleration, unexpected trajectory deviation within the elbow, and an upward inclination in erosion on the intrados. The presence of partially overlapping scratches and cracks suggests that continuous ploughing and material fracturing are significant contributors to the micro-mechanics of erosion. When comparing the intrados and extrados, the extrados exhibits longer and shallower scratches, indicating a smaller impact angle. This research provides a more comprehensive understanding of particle trajectories and erosion patterns within elbow junctions during liquid–solid flows, offering new insights into the mechanisms underpinning these processes.

## 1. Introduction

Liquid–solid flow is a prevalent phenomenon across numerous industrial applications, including petrochemical, hydraulic, and metallurgical engineering. This process notably influences the efficiency and safety of pipeline systems in these domains [1–3]. In this process, inherently, particles such as sand and debris carried by the fluid collide with the elbow wall, instigating erosion. This degradation reduces the pressure tolerance of the system, ultimately increasing risk and leading to considerable economic losses [4,5].

* Corresponding author. China National Offshore Oil Corporation Research Institute, Beijing 100028, China.
*E-mail address:* 292741807@qq.com (Z. Xie).

https://doi.org/10.1016/j.heliyon.2023.e21275
Received 17 April 2023; Received in revised form 17 October 2023; Accepted 18 October 2023
Available online 23 October 2023

Thus, a comprehensive understanding of liquid–solid flow and the resultant erosion is crucial to enhancing safety measures and minimising costs.

The majority of the existing research on liquid–solid flow is confined to the study of mixing tanks and fluidised beds, focusing on the impact of particle size, shape, and distribution on fluidisation and flow characteristics [6–8]. The studies on liquid–solid flow in pipes are primarily centred on elbow erosion [9–11]. Despite the advancement of theories explaining erosion mechanisms [12–14], these are largely based on stirring tank and jet flow tests, which allow for precise control over incident velocity and angle [15–17]. However, such theories may not be entirely applicable to pipe flow conditions.

Recent pipe flow erosion studies have predominantly utilised computational fluid dynamics (CFD), a method offering cost-saving benefits and detailed representations of flow characteristics and particle trajectories [18–20]. Dutta et al. [21,22] employed CFD simulations to analyse flow development, turbulent flow fields, and vortex structures in a 90-degree elbow, identifying the significant influence of Reynolds number and bend curvature on the turbulent flow characteristics and Dean vortex. Narayanan et al. [23] used a support vector machine-based meta-modelling approach to study the impact of various factors on turbulent behaviour in elbows, a method proving quicker and simpler than traditional CFD. Zhao et al. [24–26] simulated particle erosion in elbows under diverse flow patterns, such as gas–solid flow and annular flow, using a modified CFD method to assess erosion patterns, yielding valuable insights.

Erosion experiment studies in liquid–solid elbows have used various techniques to measure erosion. Vieira et al. [27] employed an electrical resistance (ER) probe to assess the impact of liquid flow rate, viscosity, and sand size on erosion in multi-phase annular flow. While the ER probe is highly sensitive, it is an intrusive device, disturbing the flow state near the measuring point, thus potentially skewing results. Parsi et al. [28,29] conducted experiments using an ultrasonic probe to determine erosion patterns and the influence of superficial gas and liquid velocities and particle size on elbow erosion. This non-intrusive measurement, however, offers lower accuracy. Both methods only capture thickness loss at limited points, failing to provide a comprehensive view of erosion. Wang et al. [30] used a painting-based method (paint on the eroded surface is removed) to investigate slurry erosion patterns and particle trajectories in serially mounted elbows. This method reveals the entire erosion pattern; however, it falls short in quantifying erosion magnitude. Peng et al. [31] devised a detachable test elbow with inserted specimens to measure erosion magnitude at 36 elbow locations using the weight loss method. Although this approach can provide pattern and quantitative erosion data, it does not elucidate the erosion micro-mechanism.

Analysing particle movement is crucial for understanding erosion mechanisms, as particle velocity and trajectory significantly influence erosion magnitude and location. Papini et al. [32] developed a particle launcher and executed angular particle impact experiments to study the effects of impact angle and velocity on crater morphology, enhancing the understanding of erosion mechanisms. Zang et al. [33,34] examined the surface damage of ductile materials caused by rotating particles using a modified particle launcher and found that particle rotating behaviours contribute to material removal. However, these particles were large (exceeding 5 mm) and free from liquid, making them unsuitable for liquid–solid flow studies. Farzad et al. [35,36] used particle image velocimetry (PIV) to investigate turbulence in a horizontal channel flow. However, the particles in the PIV method are extremely small and used as tracers, making this method unsuitable for erosion studies.

In summary, the existing erosion theories, based primarily on stirring tank and jet flow experimental data, are not ideally suited to pipe flow conditions. These theories do not consider flow characteristics and lack information on erosion micro-mechanisms. Numerous measurement methods have been employed to investigate erosion magnitude and pattern, yet there is a noticeable lack of experimental studies on particle trajectory in elbows within the literature. Many researchers resort to using the CFD method to depict particle trajectory due to its convenience and cost-effectiveness, although it fails to represent real-world physics.

In this study, we used high-speed camera technology to observe and record particle motion within the elbow. The erosion rate was calculated using the weight loss method, and scanning electron microscopy (SEM) was utilised to record erosion micro-morphology.

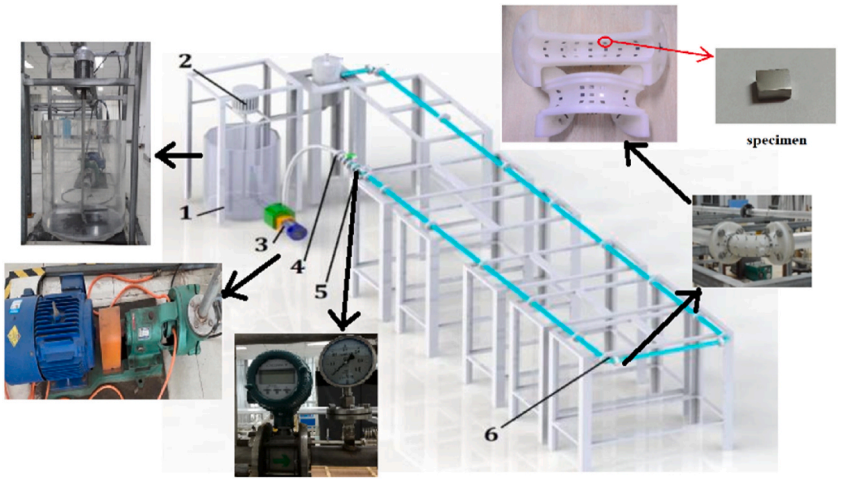


**Fig. 1.** Diagram of the liquid–solid flow experimental loop (1-water tank, 2-mixer, 3-pump, 4-check valve, 5-electromagnetic flowmeter, and 6-test elbow).

The insights garnered from these experiments provide valuable contributions to liquid–solid flow studies and erosion estimation. These findings offer guidelines to enhance the reliability and safety of liquid–solid pipeline systems.

## 2. Experimental background

### 2.1. Experimental apparatus and materials

The liquid–solid flow experimental loop utilised in this study, illustrated in Fig. 1, is based on the design developed by Peng et al. [31]. The experimental loop comprises pipelines, a water tank, a mixer, a pump, a check valve, an electromagnetic flowmeter, and a test elbow. The pipeline is fabricated from acrylic, facilitating the observation of both the flow and particle movement within it. The straight pipeline preceding the test elbow extends to 200*D* (*D* represents the pipeline's inner diameter, where $D = 50.8$ mm) to establish a fully developed flow. The water tank holds a capacity of 300 *L*, with a mixer attached to its top to ensure uniform distribution of particles in the liquid through stirring. Connected to the base of the tank is a multi-phase pump (type: 50HFM-I-25/50; manufactured by Qing Ju, China; flow rate: 5–25 $m^3$/h), which regulates flow velocity in the loop by adjusting the flow rate. The YOKOGAWA AXF040G electromagnetic flowmeter (manufactured by YOKOGAWA, Japan) measures the flow rate, with a range of 0.01 $m^3$/h to 50 $m^3$/h.

The test elbow, fabricated from acrylonitrile butadiene styrene resin, has a curvature radius of 1.5*D* and can be divided into two sections: the extrados and intrados. Thirty-six stainless steel specimens are inserted in the elbow's inner wall. Fig. 2 details the positions of these specimens within the test elbow. Along the flow direction, the radial angle between two sets of specimens is 22.5° (Fig. 2(a)). An additional set of specimens is situated 1*D* before the elbow inlet, and another set is placed 1*D* after the elbow outlet. Within one set of specimens, the circumferential angle between two specimens on the pipe's cross section is 45° (Fig. 2(b)).

To facilitate subsequent analysis, all specimens have been numbered, as shown in Fig. 3. Fig. 3(a) shows the extrados section and Fig. 3(b) shows the intrados section.

Fig. 4 illustrates a specimen mounted on the elbow. The specimen is affixed to the wall of the test elbow using a screw and nut, with the gap between the specimen and the elbow filled with 704 silica gel to prevent liquid leakage. The dimensions of the specimen are 8 mm × 6 mm × 5 mm, and the test area (the surface in contact with the fluid) encompasses 48 $mm^2$. The test surface aligns flush with the inner surface of the elbow, ensuring smooth flow. While the specimen test surface is flat, the surface adjacent to the notch is curved, resulting in a small step between the two surfaces. However, the height of the step is minor (less than 0.5 mm), and the turbulence it might cause is insignificant and can thus be disregarded.

The specimen is composed of 316L stainless steel, with a density of 7980 kg/$m^3$, a Rockwell hardness of 90, and a specific chemical composition presented in Table 1.

The experimental materials include deionised water and silicon dioxide sand (sourced from the Shengli oil field, China) serving as the liquid and particles, respectively. The sand has an average diameter of 350 μm, with its particle size distribution depicted in Fig. 5. It has a density of 2650 kg/$m^3$ and a Mohs hardness of 7. To enhance the visibility of the sand's motion, it has been coloured red.

### 2.2. Experimental process and measurement

Fig. 6 presents the experimental procedure for this study, which consists of three stages: preparation, execution, and post-processing.

In the preparation stage, prior to the experiment, test surfaces are sequentially polished with water sandpaper, ranging from 240# to 1000#. They are then cleansed with acetone and deionised water. These specimens are subsequently dried in a vacuum oven for 12 h and weighed using a Sartorius electronic balance (type: SECURA225D-1CN; manufactured by Sartorius, Germany; accuracy: 0.01 mg).

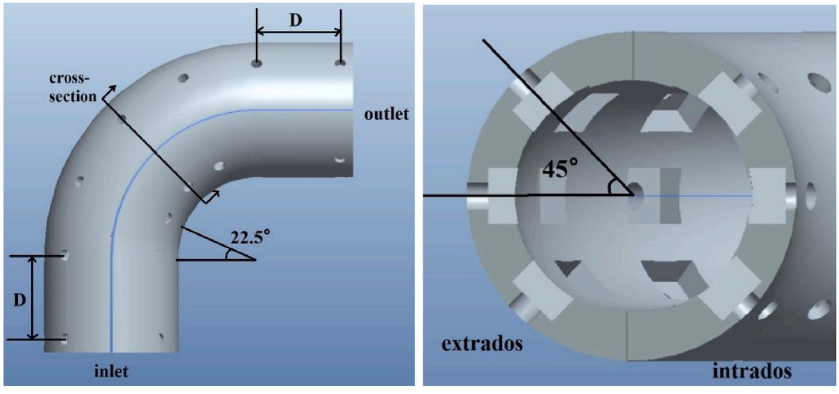


**Fig. 2.** Positions of the specimens within the test elbow ((a) top view and (b) cross-section view of the pipe).

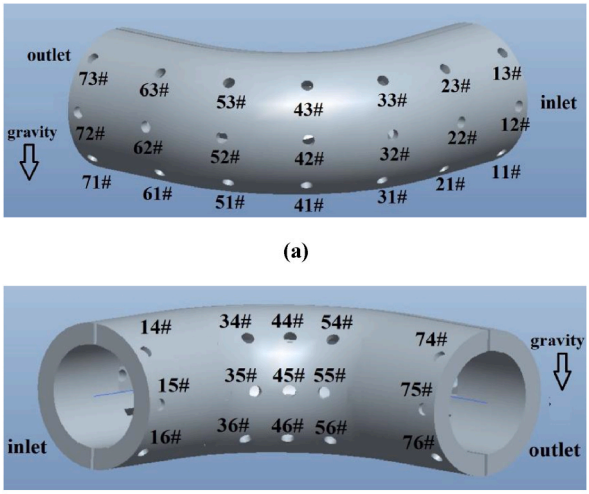


**Fig. 3.** Numbering of each specimen within the test elbow ((a) extrados section and (b) intrados section).

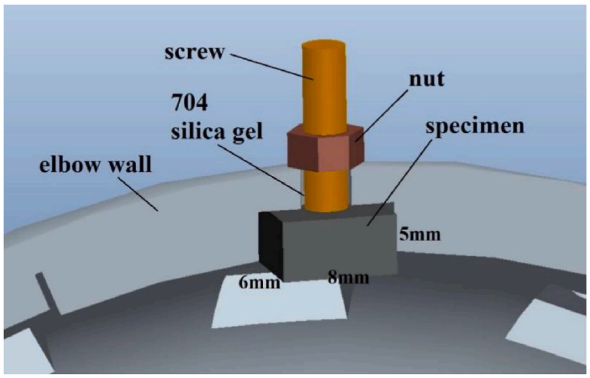


**Fig. 4.** Specimen mounted on the elbow.

**Table 1**
Chemical composition of 316L stainless steel (wt%).

| C | Si | Mn | S | P | Ni | Cr | Mo | N | Fe |
|---|---|---|---|---|---|---|---|---|---|
| 0.02 | 0.46 | 1.2 | 0.001 | 0.03 | 10.07 | 16.05 | 2.03 | 0.05 | 70.09 |

Each specimen is weighed thrice, and the average weight is recorded as its pre-experiment mass. Finally, specimens are inserted, encapsulated with 704 silica gel, and mounted on the loop.

In the execution stage, all devices are connected as depicted in Fig. 1 and verified to ensure the loop functions effectively without leakage. Sand is then introduced into the water tank. The stirring mixer facilitates the suspension of sand particles in the water, resulting in a particle concentration (by weight) of 2 %. The pump is then activated, adjusting the flow rate to 18.2 $m^3$/h, implying a pipe flow velocity of 2.5 m/s (similar to the velocity in oil pipelines). Subsequent trials with various velocities (1 m/s to 3.5 m/s) revealed that velocities below 2 m/s result in particle deposition at the pipe bottom before reaching the test elbow. Velocities exceeding 3 m/s induce small bubbles in the flow, interfering with particle motion observation. The pipe flow Reynolds number is $1.27 \times 10^5$, corresponding to a turbulent flow state.

A transparent acrylic elbow, identical in geometry to the test elbow, is utilised for observing particle motion in the elbow. A high-speed camera (type: NAC MEMRECAM HX-7; manufactured by NAC, Japan) is used to capture particle motion, with an image resolution of $1920 \times 1080$ pixels, a frame rate of 1000 fps, and an exposure time of 0.001 s. Following this, the acrylic elbow is replaced by the test elbow to perform the erosion tests, each of which spans 36 h to ensure measurable elbow erosion. The selected test conditions (sand size, particle concentration, and flow velocity) reflect production conditions in oil field pipelines.

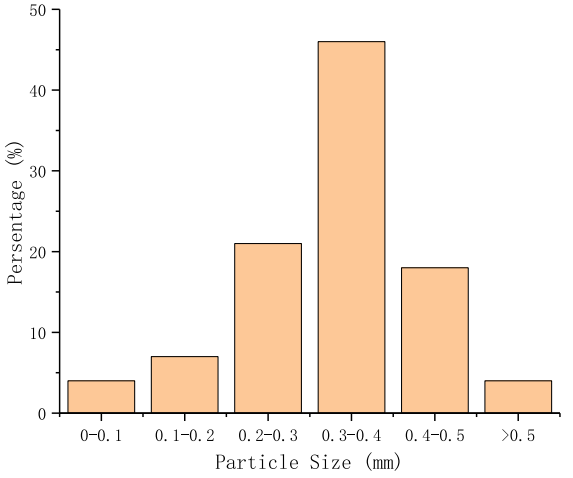


**Fig. 5.** Particle size distribution of the sand employed in this study.

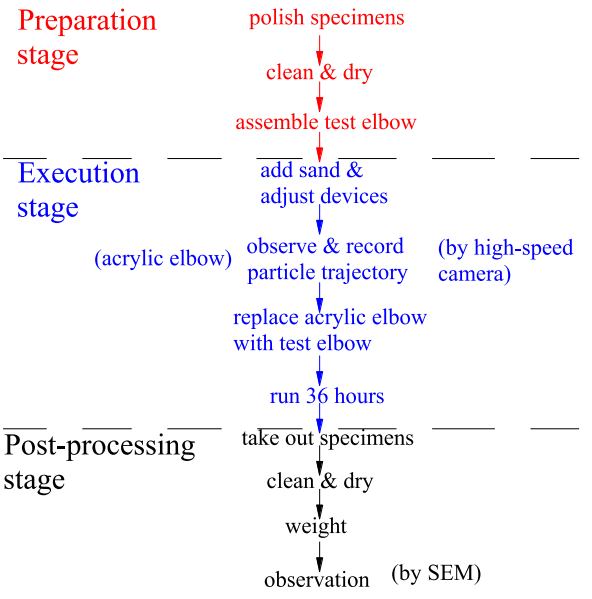


**Fig. 6.** Procedure of the experiment in this study.

In the post-processing stage, the test elbow is detached from the loop, and the specimens are extracted, cleaned with deionised water, and dried in a vacuum oven. The specimens are then weighed thrice, with the average weight being recorded as the post-experiment mass. The micro-morphology of the test surface is observed and recorded using a scanning electron microscope (type: Thermo Fisher Scientific Apreo 2; manufactured by Thermo Fisher, USA), with an accuracy of 1 nm. The erosion rate (wall thickness loss per $m^2$ per s) at various positions within the elbow is computed using the weight-loss method, described as follows:

$$ER = (w_0 - w_1) / (S \bullet t \bullet \rho_w), \quad (1)$$

where $ER$ is the erosion rate; $w_0$ and $w_1$ represent the specimen mass before and after the experiment, respectively; S is the test surface area; $t$ is the experiment duration; $\rho_w$ represents the specimen density. To minimise the potential for accidental error, each experiment was repeated three times to enhance data reliability.

## 3. Results and discussion

### 3.1. Particle movement

High-speed camera images reveal that in the liquid–solid flow, particles passing through the elbow can be classified into three categories: those moving towards the intrados, along the centre line, or towards the extrados. Fig. 7 illustrates a typical particle movement within the elbow, indicating particles within circle A moving towards the intrados, particles within circle B following the elbow centre line, and particles within circle C moving towards the extrados.

For further analysis of these particle movements, the trajectory of a single particle injected from different positions at the elbow inlet is tracked. Fig. 8 depicts the trajectory of a particle released from the centre of the elbow inlet. As shown in the figure, the particle maintains a straight path before entering the elbow (calibration tail 12 mm–16 mm), following which it moves along the elbow centre line synchronously with the liquid (calibration tail 18 mm–21 mm). As the particle reaches the elbow outlet, its trajectory reverts to a straight line (calibration tail 23 mm–26 mm).

This trajectory suggests that a particle in the pipe centre adheres closely to the liquid as it crosses the elbow, implying a strong influence of the carrying fluid on the particle. Moreover, the particle velocity increases from 2 m/s (at the elbow inlet) to 2.8 m/s (at the elbow outlet) as it passes through the elbow. This may be attributable to the specific geometric structure of the elbow, which accelerates the fluid and, consequently, the particles.

Fig. 9 illustrates the trajectory of a particle injected from the intrados side of the elbow inlet. Similar to the centre-injected particle, a particle released from the intrados side also moves in a straight line before reaching the elbow inlet (calibration tail 12 mm–17 mm). However, the particle crosses the centre line, impacts the extrados side of the elbow outlet, and then rebounds to the main stream. The deviation from the centre line becomes apparent at the elbow angle of 60° (starting from the elbow inlet), and the particle velocity increases from 2.4 m/s (at the elbow inlet) to 3.3 m/s (at the elbow outlet).

Fig. 10 depicts the trajectory of a particle released from the extrados side of the elbow inlet. In this figure, the straight particle trajectory before the elbow inlet turns towards the pipe centre and impacts the intrados side of the elbow (calibration tail 23 mm). In contrast to the previous two cases, the particle initially decelerates from 2.3 m/s (at the elbow inlet) to 1.9 m/s (at the elbow angle of 30°) but subsequently accelerates to 2.6 m/s (at the elbow outlet) while passing through the elbow. This may be due to the generation of a secondary flow perpendicular to the main stream as the fluid traverses the elbow, causing the particle to be drawn to the centre and resulting in a deviation of the particle trajectory.

Fig. 11 provides further insights into the formation of the secondary flow and particle movements within the elbow.

As shown in Fig. 11, the fluid near the extrados decelerates upon entering the elbow due to the spatial constraints imposed by the extrados wall geometry. Furthermore, the fluid near the intrados of the elbow initially accelerates as it is free from wall restrictions but subsequently slows down as it reaches the extrados. The confluence of these two fluids forms a fluid stagnation zone, as proposed by Shirazi et al. [37]. The fluid from the extrados bifurcates into two flows, circumventing the stagnation zone (obstacle) along the circumferential pipe wall as it progresses downstream. These two flows converge again at the intrados of the elbow, resulting in the secondary flow. After decelerating within the stagnation zone, the fluid from the intrados changes course and returns to the main stream.

The particle released from the extrados side (solid) initially decelerates due to the fluid stagnation area, collides with the extrados wall, and is subsequently drawn into and transported by the secondary flow to impact the intrados wall. On the other hand, the particle released from the intrados side (hollow) is initially accelerated by the faster flow, collides with the extrados wall, and is carried downstream by the main stream.

To further analyse particle movement, the Stokes number (Stk) is introduced, defined as the ratio of the particle relaxation time to the fluid characteristic time. The Stokes number represents the ratio of drag force to inertia force acting on the particle, and its formula is as follows:

$$\mathrm{Stk} = \left(\rho_{\mathrm{P}} d_{\mathrm{P}}^2 u\right) / \left(18\mu D\right), \tag{2}$$

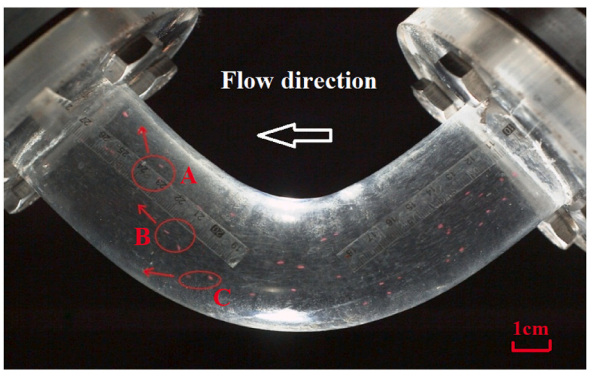


**Fig. 7.** Particle movement in liquid–solid elbow.

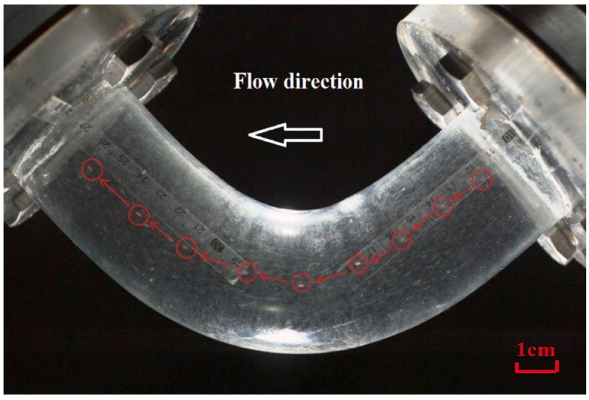


**Fig. 8.** Trajectory of the particle released from the centre of the elbow inlet.

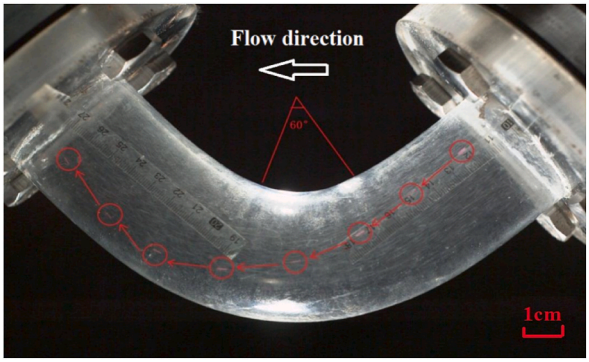


**Fig. 9.** Trajectory of the particle injected from the intrados side of the elbow inlet.

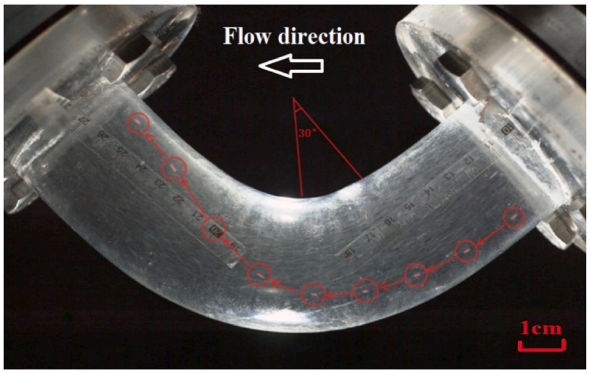


**Fig. 10.** Trajectory of the particle released from the extrados side of the elbow inlet.

where Stk is the Stokes number; $\rho_P$ is particle density; $d_p$ is the particle diameter; $u$ is the velocity of the carrier fluid; $\mu$ is the dynamic viscosity of the fluid; $D$ is the pipe diameter.

A Stokes number smaller than 1 implies that the particle closely follows the fluid. Moreover, stronger particle inertia suggests a higher likelihood of deviation from the streamline. The equation reveals that a higher velocity results in a larger Stokes number. For the centre-injected particle, the Stokes number is 0.73 (calculated using Equation (2)), signifying that the particle closely follows the elbow centre line. For the intrados-injected particle, the Stokes number is larger (0.86) (calculated using Equation (2)) due to the faster fluid velocity, resulting in a deviation from the elbow centre line. For the extrados-injected particle, the slower fluid, confined by the extrados wall, results in a smaller Stokes number (0.5) (calculated using Equation (2)). The secondary flow at this location can easily transport the particle to the intrados side of the elbow.

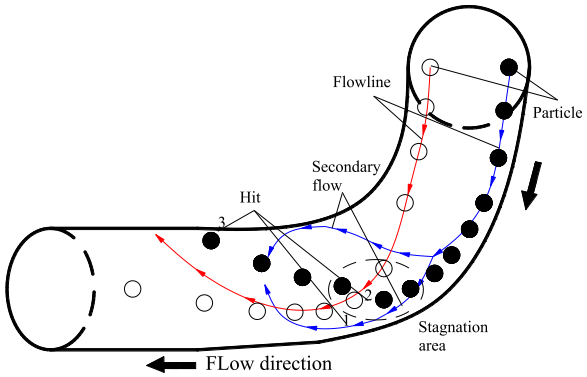


**Fig. 11.** Flowline and particle movements in the elbow.

### 3.2. Erosion analysis

Upon completion of the experiment, erosion rates at different points within the elbow were computed using the weight-loss method. The erosion rate for each specimen, calculated using Equation (1), is presented in Table 2.

The specimens corresponding to the impact points in Fig. 7 are 61#, 56#, and 76#. To further analyse the micro-mechanism of erosion at these three critical points within the elbow (similar to the findings by Wang et al. [30] and Peng et al. [31]), the surface topography of specimens 61#, 56#, and 76# were observed and recorded using SEM.

Fig. 12 presents the macro-morphology of the specimen surfaces before and after the erosion test. The figure reveals noticeable alterations to the specimen surface after erosion, with an upward incline in erosion on specimens 56# (Fig. 12(c)) and 76# (Fig. 12(d)). This pattern could potentially be influenced by the secondary flow. To examine the details, the specimens were observed using SEM.

Fig. 13 illustrates the micro-topography of the specimen surface prior to and following the erosion test. The micro-topography of the polished specimen surface, shown in Fig. 13(a), precedes the experiment and is used as a reference for subsequent comparisons.

As depicted in Fig. 13(a), the micro-morphology of the polished test surface is flat and neat, covered with parallel scratches prior to the experiment. These scratches, smaller than 5 μm, are significantly smaller than the particle size, indicating that the polished surface can accurately track the particle impact trails.

Fig. 13(b) reveals the micro-morphology of the test surface of specimen 61# after the erosion test. The initially flat surface evolved into a rugged surface covered with multiple layers of overlapping horizontal scratches. These scratches, approximately 10 μm wide—approximately 3 % of the particle size—have depths less than 3 μm.

A comprehensive analysis of these phenomena suggests that particles transported by liquid collide with the test surface at a small incident angle. The particle's normal velocity component applies downward pressure and compresses the material, forming lips (circle A in Fig. 13(b)). Concurrently, the tangential velocity component pushes the material forward, resulting in a scratch and the raised lip (circle B in Fig. 13(b)).

The formation of numerous small vortexes near the wall region cushions particles and reduces their normal velocity [27]. However, the tangential velocity component is generally larger than the normal velocity, and the damping is weaker, resulting in the depth of the scratch being substantially smaller than its width. Subsequent particles repeat this process, resulting in an overlapping scratches morphology. Furthermore, the repeated impacts compress the surface, causing the metal cells to slip and distort, making the material harder and more brittle (Fig. 14). Continuous impacts can strain the material to the point of cracking and dislodging the formed lips.

Fig. 13(c) provides a view of the micro-morphology of the test surface of specimen 56# after the erosion test. Similar to specimen 61#, the micro-morphology consists of a rugged surface covered with overlapping scratches. However, in contrast to specimen 61#, these scratches incline upwards, implying the presence of a velocity component perpendicular to the main stream in addition to the velocity component along the main stream. The shorter, deeper scratches on specimen 56# compared to those on specimen 61# suggest a larger normal velocity component and a smaller tangential velocity component, indicating a larger incident angle. Deformation and accumulation of material have also raised lips around the scratches.

Fig. 13(d) shows the micro-morphology of the test surface on specimen 76# following the erosion test. In addition to the overlapping pattern common to all three specimens, the scratches here are shorter than those on specimen 61#, implying a larger incident angle. The secondary flow plays a significant role in this phenomenon. Furthermore, a round particle impact crater is observed, suggesting the possibility of particles striking the intrados side of the elbow at a near-normal direction and high speed.

## 4. Conclusions

In this study, we examined the movement of particles introduced from different positions at the elbow inlet and subsequently analysed the micro-morphology of typical erosion surfaces to unveil the characteristics of flow and erosion micro-mechanisms in liquid–solid flow. The limitations of this study render it suitable only for scenarios involving low-speed (<3 m/s) liquid–solid pipe flow, with a Stokes number not exceeding 1. The primary conclusions are summarised as follows:

**Table 2**
Erosion rates for each specimen using the weight loss method.

| Specimen number | Mass lost (mg) | Erosion rate ( $\times 10^{-8}$ mm/s) | Specimen number | Mass lost (mg) | Erosion rate ( $\times 10^{-8}$ mm/s) |
|---|---|---|---|---|---|
| 11# | 0.87 | 1.76 | 44# | 0.37 | 0.74 |
| 12# | 0.06 | 0.13 | 45# | 0.03 | 0.06 |
| 13# | 0.12 | 0.24 | 46# | 3.15 | 6.34 |
| 14# | 0.21 | 0.43 | 51# | 5.27 | 10.62 |
| 15# | 0.63 | 1.26 | 52# | 3.69 | 7.43 |
| 16# | 1.23 | 2.47 | 53# | 2.18 | 4.40 |
| 21# | 0.61 | 1.23 | 54# | 0.81 | 1.64 |
| 22# | 0.30 | 0.61 | 55# | 0.03 | 0.07 |
| 23# | 0.06 | 0.12 | 56# | 9.31 | 18.76 |
| 31# | 1.49 | 3.00 | 61# | 10.87 | 21.90 |
| 32# | 0.90 | 1.81 | 62# | 8.69 | 17.50 |
| 33# | 0.46 | 0.93 | 63# | 3.96 | 7.98 |
| 34# | 0.05 | 0.11 | 71# | 6.78 | 13.65 |
| 35# | 0.06 | 0.12 | 72# | 3.52 | 7.09 |
| 36# | 0.17 | 0.35 | 73# | 2.30 | 4.63 |
| 41# | 3.12 | 6.29 | 74# | 2.05 | 4.13 |
| 42# | 2.31 | 4.66 | 75# | 2.61 | 5.26 |
| 43# | 0.95 | 1.92 | 76# | 8.73 | 17.59 |

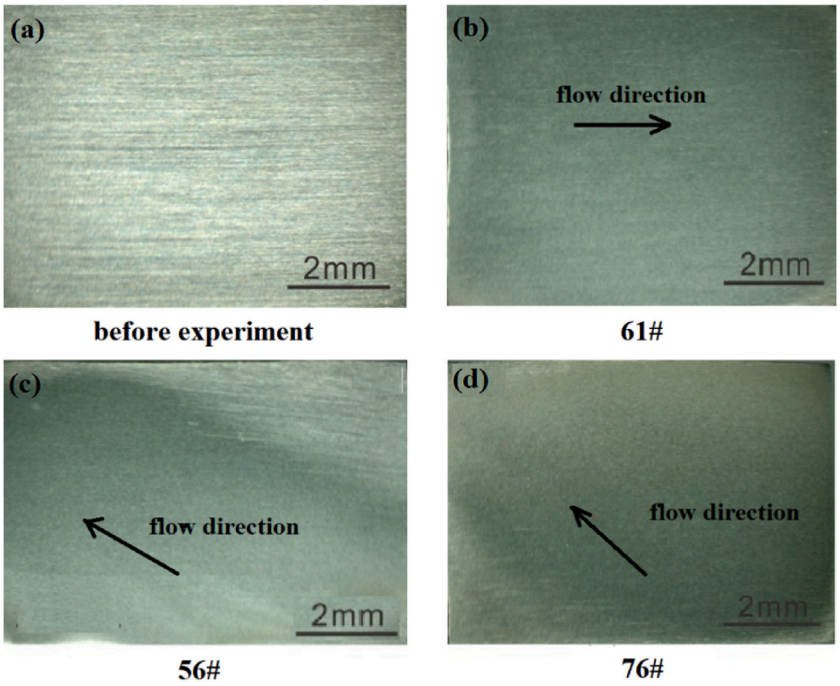


**Fig. 12.** Macro-morphology of the specimen surfaces before and after erosion test.

(1) In low-speed (2.5 m/s) liquid–solid flow, particles injected from the inlet centre follow the elbow centre line. Particles introduced from the inlet intrados side noticeably deviate from the centre line at an elbow angle of 60° (from the inlet), whereas those released from the extrados deviate towards the intrados side at an elbow angle of 30°. Secondary flow plays a significant role in both particle acceleration and the unexpected trajectory deviation within the elbow.
(2) Fluid near the extrados decelerates due to the confined wall geometry, subsequently bifurcating into two flows that circumvent the stagnation zone (obstacle) along the circumferential pipe wall while continuing downstream. These two flows converge at the elbow intrados, forming a secondary flow, which influences the formation of upwardly inclined erosion on the intrados of the elbow.
(3) At the typical positions on the elbow (middle and bottom of extrados, elbow outlet intrados), the presence of partially overlapping scratches and cracks indicates that continuous impacts compress the surface, causing metal cells to slip and distort. This, in turn, leads to the generation of cracks and the shedding of the accumulated lips, culminating in the development of erosion micro-mechanism.

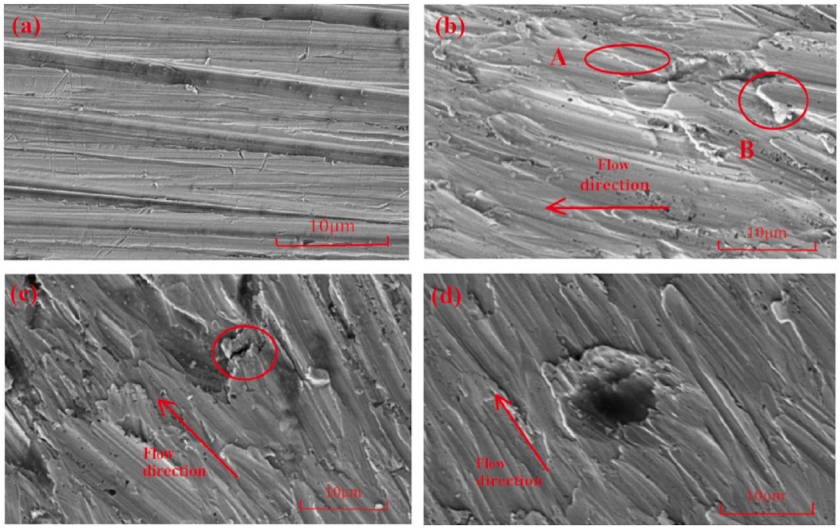


**Fig. 13.** Micro-topography of the specimen surfaces before and after erosion test ((a) before test, (b) specimen 61# after test, (c) specimen 56# after test, and (d) specimen 76# after test).

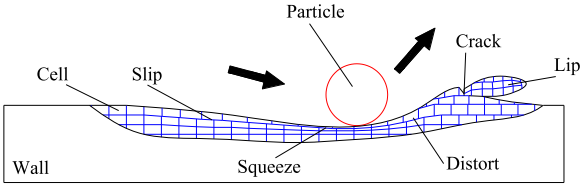


**Fig. 14.** Micro-mechanism of the particle erosion process.

## Data availability statement

Sharing research data helps other researchers evaluate your findings, build on your work and to increase trust in your article. We encourage all our authors to make as much of their data publicly available as reasonably possible. Please note that your response to the following questions regarding the public data availability and the reasons for potentially not making data available will be available alongside your article upon publication.

## CRediT authorship contribution statement

**Zhenqiang Xie:** Conceptualization, Formal analysis, Investigation, Writing – original draft, Writing – review & editing. **Xuewen Cao:** Conceptualization, Funding acquisition. **Qingping Li:** Data curation, Formal analysis, Supervision. **Haiyuan Yao:** Data curation, Formal analysis, Funding acquisition. **Rui Qin:** Formal analysis. **Xiaoyang Sun:** Data curation, Methodology, Writing – review & editing.

## Declaration of competing interest

The authors declare that they have no known competing financial interests or personal relationships that could have appeared to influence the work reported in this paper.

## Acknowledgements

The authors would like to thank everyone who supported this research. This research received financial support from the National Natural Science Foundation of China (Grant No. U21B2065) and National Natural Science Foundation of China (Grant No. 51874340).

## References

[1] S. Vishnuvardhan, A. Murthy, A. Choudhary, A review on pipeline failures, defects in pipelines and their assessment and fatigue life prediction methods, Int. J. Pres. Ves. Pip. 201 (2023), 104853.

[2] K. Mishima, M. Ishii, Flow regime transition criteria for upward two-phase flow in vertical tubes, Int. J. Heat Mass Tran. 27 (5) (1984) 723–737.
[3] S. Wang, S. Guo, J. Gao, X. Lan, Q. Dong, X. Li, Simulation of flow behavior of liquid and particles in a liquid–solid fluidized bed, Powder Technol. 224 (2012) 365–373.
[4] B. Wu, M. Firouzi, T. Mitchell, T.E. Rufford, C. Leonardi, B. Towler, A critical review of flow maps for gas-liquid flows in vertical pipes and annuli, Chem. Eng. J. 326 (2017) 350–377.
[5] M. Parsi, K. Najmi, F. Najafifard, S. Hassani, B.S. Mclaury, S.A. Shirazi, A comprehensive review of solid particle erosion modeling for oil and gas wells and pipelines applications, J. Nat. Gas Sci. Eng. 21 (2014) 850–873.
[6] M.T. Islam, A.V. Nguyen, Effect of particle size and shape on liquid-solid fluidization in a HydroFloat cell, Powder Technol. 379 (2021) 560–575.
[7] Z. Yuan, S. Wang, B. Shao, X. Chen, L. Xie, J. Fan, Simulation study on the flow behavior of wet particles in the power-law liquid-solid fluidized bed, Powder Technol. 415 (2023), 118117.
[8] J. Feng, S. Yan, G. Qi, X. Li, Particle distribution and pressure drop in a horizontal two-pass liquid-solid circulating fluidized bed heat exchanger, Powder Technol. 416 (2023), 118210.
[9] V. Kannojiya, M. Deshwal, D. Deshwal, Numerical analysis of solid particle erosion in pipe elbow, Mater. Today. Proc. 5 (2018) 5021–5030.
[10] P. Zahedi, M. Parsi, A. Asgharpour, B.S. McLaury, S.A. Shirazi, Experimental investigation of sand particle erosion in a 90° elbow in annular two-phase flows, Wear 438–439 (2019), 203048.
[11] R. Zhang, D. Zhu, H. Liu, Y. Liu, Random process of particle-wall collision and its application in numerical simulation of solid particle erosion, Wear 452–453 (2020), 203288.
[12] H.C. Meng, K.C. Ludema, Wear models and predictive equations: their form and content, Wear 181– 183 (1995) 443–457.
[13] G. Sundararajan, A comprehensive model for the solid particle erosion of ductile materials, Wear 149 (1–2) (1991) 111–127.
[14] Y.I. Oka, K. Okamura, T. Yoshida, Practical estimation of erosion damage caused by solid particle impact: Part 1: effects of impact parameters on a predictive equation, Wear 259 (1) (2005) 95–101.
[15] R. Fishwick, M. Winterbottom, D. Parker, X. Fan, H. Stitt, The use of positron emission particle tracking in the study of multiphase stirred tank reactor hydrodynamics, Can. J. Chem. Eng. 83 (1) (2005) 97.
[16] G.R. Desale, B.K. Gandhi, S.C. Jain, Improvement in the design of a pot tester to simulate erosion wear due to solid–liquid mixture, Wear 259 (2005) 196–202.
[17] C.A. Shook, M. McKibben, M. Small, Experimental investigation of some hydrodynamic factors affecting slurry pipeline wall erosion, Can. J. Chem. Eng. 68 (1990) 17–23.
[18] M. Agrawal, S. Khanna, A. Kopliku, T. Lockett, Prediction of sand erosion in CFD with dynamically deforming pipe geometry and implementing proper treatment of turbulence dispersion in particle tracking, Wear 426 (2019) 596–604.
[19] W. Peng, X. Cao, Numerical simulation of solid particle erosion in pipe bends for liquid–solid flow, Powder Technol. 294 (2016) 266–279.
[20] A. Mansouri, H. Arabnejad, S. Karimi, S.A. Shirazi, B.S. McLaury, Improved CFD modeling and validation of erosion damage due to fine sand particles, Wear 338 (2015) 339–350.
[21] P. Dutta, H. Chattopadhyay, N. Nandi, Numerical studies on turbulent flow field in a 90 deg pipe bend, J. Fluid Eng-T ASME 144 (2022), 061104.
[22] P. Dutta, N. Nandi, Numerical analysis on the development of vortex structure in 90 pipe bend, Prog. Comput. Fluid Dynam. Int. J. 21 (5) (2021) 261–273.
[23] G. Narayanan, M. Joshi, P. Dutta, K. Kalita, PSO-tuned support vector machine metamodels for assessment of turbulent flows in pipe bends, Eng. Comput. 37 (3) (2020) 981–1001.
[24] X. Zhao, X. Cao, Z. Xie, H. Cao, C. Wu, J. Bian, Numerical study on the particle erosion of elbows mounted in series in the gas-solid flow, J. Nat. Gas Sci. Eng. 99 (2022), 104423.
[25] X. Zhao, X. Cao, H. Cao, J. Zhang, J. Zhang, W. Peng, J. Bian, Numerical study of elbow erosion due to sand particles under annular flow considering liquid entrainment, Particuology 76 (2023) 122–139.
[26] X. Zhao, X. Cao, J. Zhang, H. Cao, J. Zhang, W. Peng, J. Bian, Experimental and numerical investigation of erosion in plugged tees for liquid-solid flow, Int. J. Multiphas. Flow 160 (2023), 104348.
[27] R.E. Vieira, M. Parsi, P. Zahedi, B.S. McLaury, S.A. Shirazi, Electrical resistance probe measurements of solid particle erosion in multiphase annular flow, Wear (2017) 15–28, 382–383.
[28] M. Parsi, R.E. Vieira, N. Kesana, B. McLaury, S. Shirazi, Ultrasonic measurements of sand particle erosion in gas dominant multiphase flow, Wear (2015) 401–413, 328–329.
[29] R.E. Vieira, M. Parsi, P. Zahedi, B.S. McLaury, S.A. Shirazi, Ultrasonic measurements of sand particle erosion under upward multiphase annular flow conditions in a vertical-horizontal bend, Int. J. Multiphas. Flow 93 (2017) 48–62.
[30] Q. Wang, Q. Huang, N. Wang, Y. Wen, X. Ba, X. Sun, J. Zhang, S. Karimi, S.A. Shirazi, An experimental and numerical study of slurry erosion behavior in a horizontal elbow and elbows in series, Eng. Fail. Anal. 130 (2021), 105779.
[31] W. Peng, X. Cao, J. Hou, K. Xu, Y. Fan, S. Xing, Experiment and numerical simulation of sand particle erosion under slug flow condition in a horizontal pipe bend, J. Nat. Gas Sci. Eng. 76 (2020), 103175.
[32] M. Papini, J.K. Spelt, Impact of rigid angular particles with fully-plastic targets Part I: analysis, Int. J. Mech. Sci. 42 (5) (2000) 991–1006.
[33] X. Zang, X. Cao, J. Zhang, Z. Xie, N. Xiong, F. Darihaki, J. Bian, Investigation of surface damage of ductile materials caused by rotating particles, Wear 488 (2022), 204185.
[34] Z. Xie, X. Cao, C. Fu, J. Zhang, X. Sun, C. Wu, X. Zhao, Experimental study on the repeated impact of sharp particles on metal surface, 474–475, Wear (2021), 203716.
[35] A. Farzad, E. Masoud, R.S. Sanders, G. Sina, Particle image and tracking velocimetry of solid-liquid turbulence in a horizontal channel flow, Int. J. Multiphas. Flow 112 (2019) 83–99.
[36] C.J. Khler, S. Scharnowski, C. Cierpka, On the uncertainty of digital PIV and PTV near walls, Exp. Fluid 52 (6) (2012) 1641–1656.
[37] S.A. Shirazi, J.R. Shadley, B.S. McLaury, E.F. Rybicki, A procedure to predict solid particle erosion in elbows and tees, J. Pressure Vessel Technol. 117 (1995) 45–52.